
Article:
Maguire, J.M., Sharp, N.D., Pipes, R.B. et al. (1 more author) (2022) Advanced process simulations for thick-section epoxy powder composite structures. Composites Part A: Applied Science and Manufacturing, 161. 107073. ISSN 1359-835X

https://doi.org/10.1016/j.compositesa.2022.107073

Composites: Part A 161 (2022) 107073

Contents lists available at ScienceDirect

Composites Part A

journal homepage: www.elsevier.com/locate/compositesa

Advanced process simulations for thick-section epoxy powder composite structures

James M. Maguire [a,*], Nathan D. Sharp [b], R. Byron Pipes [b], Conchúr M. Ó Brádaigh [a]

[a] School of Engineering, Institute for Materials and Processes, The University of Edinburgh, Edinburgh EH9 3FB, UK
[b] Composites Manufacturing and Simulation Center, Purdue University, Indiana Manufacturing Institute, 1105 Challenger Drive, West Lafayette IN 47906, USA

ARTICLE INFO

Keywords:
A. Epoxy powder
C. Finite element analysis (FEA)
C. Process simulation
E. Out of autoclave processing

ABSTRACT

Numerical modelling is used to perform process simulations for thick-section composite laminates. Three forms of laminate are used to illustrate how thermal and cure gradients can be reduced by choice of thermal cycle. Low exotherm epoxy powders with the vacuum bag process have shown success in both glass and carbon fiber systems and the results presented in the present work show how the optimum thermal cycle can be determined. The three laminate geometries investigated in the present study included: a one-dimensional flat laminate, a three-dimensional flat laminate, and an axisymmetric section of the cylindrical root of a typical wind turbine blade. Further, energy efficient and cost-effective alternative heating methods are explored.

1. Introduction

Advanced composite materials have become popular for manufacturing large load-bearing structures due to their high stiffness/strength to weight ratio and the need for increased energy efficiency in the energy and transport sectors. In the case of renewable energy, the ever-increasing span of wind turbine blades, and the advent of tidal turbines, have created challenges for composite manufacturers. To resist the loads and moments that these blades undergo, composite laminates up to 100 mm thick are required at the blade root. Such thick sections are notoriously difficult to process with conventional thermoset systems due to the heat generated when they are cured, which can be dangerous if left uncontrolled [1,2]. Moreover, the build-up of heat when manufacturing thick-section spar caps can create waves (warpage) that significantly impact the fatigue life of blades [3]. Such is the importance of this manufacturing challenge, some blade manufacturers prioritise the investigation of laminate thickness effects for the final blade design along with seawater conditioning and other important considerations such as ply-drops and bolt holes [4].

Thick sections can be processed using many of the conventional composite manufacturing techniques, however, in the case of large structures, such as wind turbine blades, vacuum assisted resin transfer moulding (VARTM) has been widely adopted as a cost effective method. One limitation of this technology is that it requires a significant level of expertise in designing appropriate flow strategies so that defects, such as dry spots, do not form [5]. To reduce complexity, the manufacturing of thicker sections can be carried out separately in a prefabrication process, and then incorporated into the whole blade assembly during infusion of the skins [2,6,7].

For the prefabrication of thick-section parts, vacuum-bag-only (VBO) prepregs, also known as out-of-autoclave (OoA) prepregs, are an effective alternative to VARTM. These material systems include partially impregnated prepregs (a.k.a. 'semi-pregs'), and fully impregnated prepregs with some additional microstructure to allow for air evacuation [8]. Compared to VARTM, the resin infusion process is less complex because the resin is only required to flow through-thickness into the adjacent dry fibre tows. Within the marine and wind energy sector, several companies have developed such material systems for the manufacture of blade roots, skins and spars [9]. In the case of Hexcel's M79 system, they developed a 'low-exotherm' epoxy resin to address the challenge of controlling the exothermic curing reaction in thick-section components [10].

Low-exotherm thermosetting formulations offer a significant processing advantage in manufacturing thick-section structures, however, the literature on this subject is sparse. Hexcel is one of the few companies to release any technical publications on the development of these systems for thick-section composites, and they have shown that it is possible to manufacture "ultra thick" laminates using their low-exotherm VBO prepreg [10]. One type of resin system which has the potential to be used for low-exotherm VBO prepregs is epoxy powder [11]. In addition to the VBO prepregs already mentioned,

* Corresponding author.
E-mail address: jmaguir4@ed.ac.uk (J.M. Maguire).

https://doi.org/10.1016/j.compositesa.2022.107073
Received 9 May 2022; Received in revised form 8 July 2022; Accepted 9 July 2022
Available online 16 July 2022

Nomenclature

α	Degree of cure (DoC)
α_c	Temperature-dependent critical DoC
α_g	DoC at gelation
β	Degree of impregnation
η	Viscosity [Pa s]
η_{g0}	Viscosity of the uncured resin [Pa s]
θ	Ply angle [°]
κ	Thermal conductivity matrix [W/m K]
κ_{UD}	Orthogonal thermal conductivity matrix for unidirectional plies [W/m K]
κ_θ	Thermal conductivity matrix for off-axis plies [W/m K]
$\kappa_{c,L}$	Longitudinal thermal conductivity of the impregnated fabric [W/m K]
$\kappa_{c,T}$	Transverse thermal conductivity of the impregnated fabric [W/m K]
$\kappa_{f,L}$	Longitudinal thermal conductivity of the fibre [W/m K]
$\kappa_{f,T}$	Transverse thermal conductivity of the fibre [W/m K]
κ_{fab}	Thermal conductivity of the dry fabric [W/m K]
κ_r	Thermal conductivity of the epoxy, [W/m K]
$\kappa_{r,liq}$	Thermal conductivity of the liquid epoxy [W/m °C]
$\kappa_{r,pow}$	Thermal conductivity of the epoxy powder [W/m K]
κ_{XX}	Longitudinal thermal conductivity [W/m K]
κ_{YY}	Transverse thermal conductivity [W/m K]
κ_{ZZ}	Effective through-thickness thermal conductivity [W/m K]
λ	Fitting constant for DiBenedetto model
ρ_c	Consolidated ply density [kg/m^3]
ρ_{ply}	Ply density [kg/m^3]
ρ_f	Fibre density [kg/m^3]
ρ_r	Resin density [kg/m^3]
$\rho_{r,cur}$	Cured resin density [kg/m^3]
φ	Resin volume fraction/Total ply porosity
φ_1	Inter-tow porosity
φ_2	Intra-tow porosity
φ_{fab}	Porosity of the fabric layer
χ	Powder void fraction during sintering
χ_0	Initial powder void fraction of the powder
χ_E	Pre-exponential rate constant for sintering
χ_∞	Final powder void fraction during sintering
A	Fitting constant for viscosity model
A_α	Pre-exponential constant [s^{-1}]
B	Fitting constant for sintering model
C	Diffusion constant for cure kinetics model
$c_{P,c}$	Specific heat capacity of the composite [J/kg K]
$c_{P,r}$	Specific heat capacity of epoxy [J/kg °C]
$c_{P,f}$	Specific heat capacity of fibre [J/kg K]
$C_{\eta 1}$	Fitting constant for viscosity model
$C_{\eta 2}$	Fitting constant for viscosity model [K]
$C_{\chi 1}$	Fitting constant for sintering model
$C_{\chi 2}$	Fitting constant for sintering model [K]
E_α	Activation energy [J/mol]
h_c	Consolidated ply thickness (a.k.a. cure ply thickness) [m]
h_{ply}	Ply thickness [m]
h_{fab}	Thickness of the fabric layer [m]
h_r	Thickness of resin layer [m]
h_r^*	Thickness of the resin layer when it is fully sintered [m]
$h_{r,0}^*$	Characteristic thickness of the resin volume
H_T	Total enthalpy of reaction [J/g]
K_1	Inter-tow permeability [m^2]
K_2	Intra-tow permeability [m^2]
k_α	Cure rate constant [s^{-1}]
L_1	Characteristic length of the inter-tow porous medium [m]
l	Impregnated layer thickness [m]
m	Reaction order
n	Reaction order
P_{app}	Applied pressure [Pa]
R	Universal gas constant [J/mol K]
R_{fib}	Fibre radius [m]
T	Temperature [K]
T_g	Glass transition temperature [K]
T_{g0}	Initial glass transition temperature of the uncured resin [°C]
$T_{g\infty}$	Glass transition temperature of the fully cured resin [°C]
T_θ	Onset temperature for melting [K]
t	Time [s]
V_f	Fibre volume fraction
$V_{f,tow}$	Fibre volume fraction of fibre tow

ÉireComposites Teo. have developed a low-exotherm VBO prepreg system based on epoxy powder technology from the powder coating industry. In the past, ÉireComposites Teo. were able to manufacture 12.6 m wind turbine blades using the epoxy powder semi-preg (partially impregnated prepreg) in combination with their patented integrally-heated ceramic tooling [12,13].

As part of the European Framework projects, MARINCOMP and POWDERBLADE, significant research has been carried out to assist with the development of this powder-based VBO prepreg system [11,14–18]. In relation to process modelling and simulation, previous investigations focussed on describing the system in a one-dimensional (1D) space i.e. through-thickness resin flow and heat transfer [14,15]. It has been demonstrated by others [19,20] that resin flow within VBO prepregs can described using 1D resin flow models based on Darcy's Law [21], while 1D (through-thickness) heat transfer has been a common assumption in the literature since the 1980s and 1990s when modelling the manufacture of thick-section composites [22–25]. The basis for this latter assumption was that the in-plane dimensions of a laminate/part were sufficiently large such that edge effects were negligible and that the temperature cycle should depend on the conditions at the centre of the laminate. Naturally, however, such assumptions are not always valid. Numerous studies have developed 2D and 3D models for thick-section composites which investigate in-plane heat conduction and more complex geometries, such as right angle bends and tapered sections, [2,26–31]. While some initial models were developed using finite difference schemes [26], later work began to focus more closely on implementing finite element schemes to numerically solve the process models [27,32]. As commercial finite element software became more advanced, some authors identified the potential of these codes for performing composite processing simulations in a more efficient and effective manner than trying to develop their own finite element codes [28,29,33–36]. In this regard, a key feature of some commercial software is the ability to augment numerical calculations with user-based subroutines, which could describe additional phenomena, such as cure kinetics [27,28,37].

In this paper, a commercial finite element analysis (FEA) software, Abaqus FEA, was used to perform 1D and 3D simulations of thick-section processing with powder-based VBO materials. A methodology is described for implementing various process models and material models within a coupled temperature-displacement analysis using user-defined subroutines. The accuracy of the simulation tool is validated via comparison with 1D experiments, and the convergence of solutions is tested

for a range of time step sizes and element sizes. Simulations are performed for 3D geometries, including the tapered root section of a wind turbine blade. The influence of anisotropic thermal conductivities is investigated for in-plane heating, and the validity of the 1D assumption is tested for different cases. Additional simulations are performed to optimise the temperature cycle and explore the use of alternative heating methods.

2. Methodology

2.1. Brief description of the material models and process models

For the powder-based VBO material investigated in this study (see Fig. 1), experimentally validated process models have already been developed to describe through-thickness heat transfer, resin flow and thickness change; an in-depth description of which can be found in Maguire et al. [14,15]. In this instance, a brief description of the associated models is provided.

As shown in Fig. 1(a), this material system is typically processed in one of two formats: semi-preg (i.e. plies that have been partially impregnated with epoxy powder in an automated process) or loose plies of fabric with epoxy powder manually dispersed between them. In both cases, heat transfer is described using the well-known heat equation, which includes a heat generation term to account for the curing reaction,

$$\rho_{ply} c_{P,c} \frac{dT}{dt} = \kappa \nabla^2 T + (1 - V_f)\rho_r H_T \frac{d\alpha}{dt} \tag{1}$$

where ρ_{ply} is ply density [kg/m^3], $c_{P,c}$ is specific heat capacity of the composite [J/kg K], T is temperature [K], κ is thermal conductivity matrix [W/m K],V_f is the fibre volume fraction, ρ_r is the resin density [kg/m^3], H_T is the total enthalpy of the curing reaction [J/g], and α is the degree of cure (DoC).

Some of the variables and parameters in Eq. (1) may vary as a function of several factors including temperature, degree of cure, degree of impregnation, powder void fraction, fibre orientation, etc. These dependencies are expanded here where necessary, however, in the context of epoxy powder composites, further understanding can be elucidated from [14]. The density and thermal conductivity of a powder-based VBO ply are dependent on its microstructure, e.g. density and thermal conductivity differ for sintered epoxy and un-sintered epoxy and they depend on the degree of impregnation of the epoxy into the fabric. For resin flow and heat transfer in the through-thickness direction, this microstructure can be simplified as layers in series with representative thicknesses (see Fig. 1(c)), e.g. a resin layer with thickness, h_r [m], a fabric layer with thickness, h_{fab} [m], and an impregnated composite layer with thickness, l [m]. In this approach, it is assumed that the ply is a closed system (i.e. there is no global through-thickness resin flow, only localised flow) and there is no in-plane resin flow. This assumption is justified on the basis of experimental observation [15] – for well distributed epoxy powder, resin flow is predominantly into the adjacent dry fabric layer, in the through-thickness direction. As such, the density of the ply, ρ_{ply} [kg/m^3], will vary as function of its thickness, h_{ply} [m], at any time, t [s],

$$\rho_{ply} = \rho_c \frac{h_c}{h_{ply}} \tag{2}$$

where ρ_c is the density of the fully consolidated ply [kg/m^3], and h_c is the thickness of the fully consolidated ply [m]. In this context, fully consolidated means the epoxy is fully sintered and the fabric layer is fully impregnated. Both of these parameters (ρ_c and h_c) can be measured experimentally for individual material systems, or can be calculated for a known fibre volume fraction (i.e. via rule of mixtures) and areal fabric weight. For this paper, h_c was measured experimentally, and ρ_c was calculated using Eq. (A.3) in Table A.1 in Appendix A. Supplementary material.

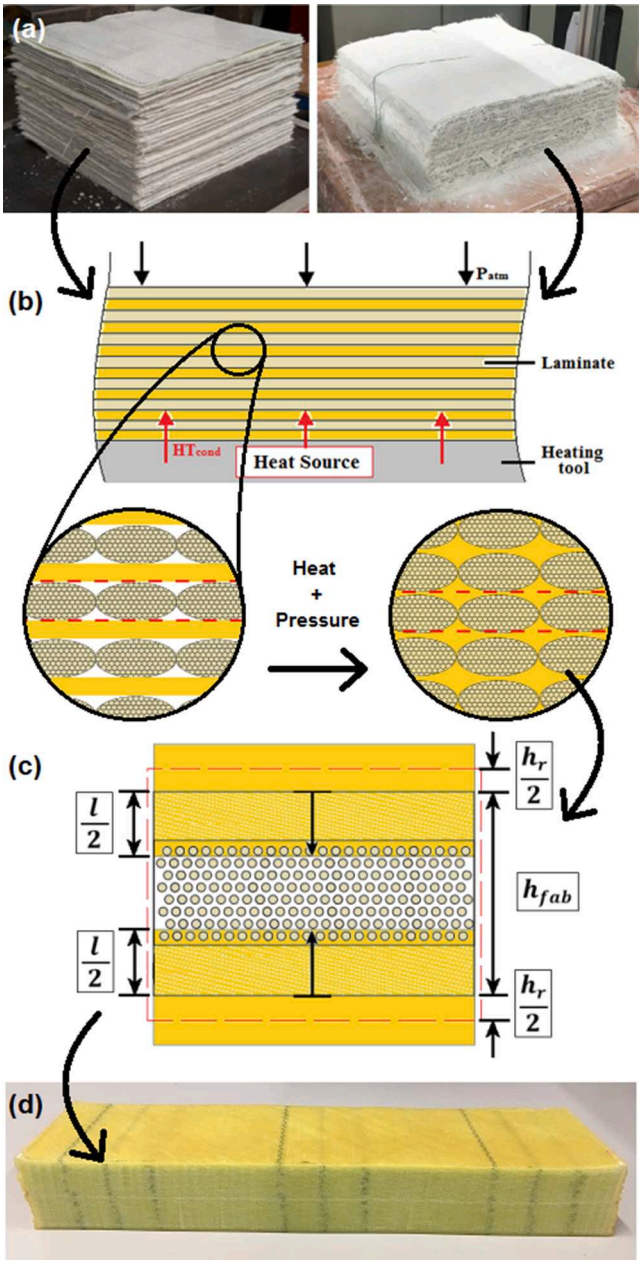

Fig. 1. (a) Two formats of glass-fibre/epoxy-powder: (left) a stack of semi-preg, (right) dry fabric manually distributed between layers. (b) Schematic representation of the alternating layers of resin and fabric, with magnification of the plies before and after heat and pressure are applied. (c) Schematic of the simplified ply microstructure used to describe resin flow. The element boundary is represented by the dashed red line. Note the porous layers are in series (i.e. 1D dual scale flow); diagonal hatching for the inter-tow region, and circle pattern for the intra-tow region. (d) A cut-section from a fully consolidated laminate manufactured using semi-preg. This figure has been . adapted from [14,15]

Knowledge of the individual layer thicknesses (i.e. h_r,h_{fab} and l) also allows for an effective through-thickness thermal conductivity, κ_{ZZ} [W/m K], to be back-calculated based on thermal resistances in series,

$$\kappa_{ZZ} = h_{ply}\left(\frac{h_r}{\kappa_r} + \frac{h_{fab} - l}{\kappa_{fab}} + \frac{l}{\kappa_{c,T}}\right)^{-1} \tag{3}$$

where κ_r is the thermal conductivity of the epoxy [W/m K] (described by Eq. (A.6) in Table A.2 in Appendix A. Supplementary material [39,40,41,42,43]), κ_{fab} is the thermal conductivity of the dry fabric [W/

m K] (see Table A.3 in Appendix A. Supplementary material [44,45,46,47]), and $\kappa_{c,T}$ is the through-thickness thermal conductivity of the impregnated fabric [W/m K] (described using a model developed by Clayton [38] – Eq. (A.2) in Appendix A Supplementary material).

For geometries where in-plane heat conduction is considered (i.e. 3D geometries), Eq. (3) forms part of the thermal conductivity matrix, κ [32]. In the case of unidirectional (UD) plies, κ is an orthogonal matrix, κ_{UD},

$$\kappa_{UD} = \begin{bmatrix} \kappa_{XX} & 0 & 0 \\ 0 & \kappa_{YY} & 0 \\ 0 & 0 & \kappa_{ZZ} \end{bmatrix} \tag{4}$$

It is assumed that, for a UD ply, the thermal conductivity in the Y direction (i.e. transverse), κ_{YY} [W/m K], is approximately equal to κ_{ZZ}. The thermal conductivity in the X direction (i.e. longitudinal), κ_{XX} [W/m K], is calculated using a rule of mixtures approach (Eq. (A.1) in Appendix A. Supplementary material, where $\kappa_{XX} = \kappa_{c,L}$).

For plies with an angle,θ [°], the thermal conductivity matrix is transformed as follows [32],

$$\kappa_\theta = \mathbf{R}^{\mathrm{T}} \kappa_{UD} \mathbf{R}, \quad \text{where } \mathbf{R} = \begin{bmatrix} \cos\theta & \sin\theta & 0 \\ -\sin\theta & \cos\theta & 0 \\ 0 & 0 & 1 \end{bmatrix} \tag{5}$$

Under vacuum conditions, it is assumed that the specific heat capacity of the material only depends on the ratio of fibres to resin. As such, the specific heat capacity of the composite, $c_{P,c}$ is determined using a rule of mixtures (ROM) approach (Eq. (A.4), Table A.1 in Appendix A. Supplementary material). The fibre volume fraction is based on a predetermined amount of powder being deposited on the reinforcing fabric and the assumption that the epoxy does not bleed significantly from the laminate during processing.

Values for the density, specific heat capacity, and thermal conductivity of the resin and fibres are taken from material data sheets and the literature; see Table A.2 and Table A.3 in Appendix A. Supplementary material.

To solve Eqs. (2) and (3), it is also necessary to model resin flow and powder sintering, and to have expressions that can describe the microstructure shown in Fig. 1(c). Beginning with the latter, the microstructure, at any time, t, is described by,

$$h_{ply} = h_{fab} + h_r \tag{6}$$

$$h_{fab} = h_c \left(\frac{1-\varphi}{1-\varphi_{fab}} \right) \tag{7}$$

$$h_r = \frac{h_r^*}{1-\chi} \tag{8}$$

where φ is the resin volume fraction (determined by the amount of powder deposited on the fabric – similar to V_f), φ_{fab} is the porosity of the fabric (described by Eq. (A.9) in Appendix A. Supplementary material), h_r^* is the thickness of the resin layer when it is fully sintered [m], and χ is the powder void fraction.

The powder void fraction, χ, is modelled using the following semi-empirical equation developed in [14],

$$\frac{d\chi}{dt} = -\chi_E \exp\left(\frac{C_{\chi 1}[T - T_\theta]}{C_{\chi 2} + T - T_\theta} \right) (\chi - \chi_\infty)^B \tag{9}$$

where χ_E is a pre-exponential rate constant, χ_∞ is the powder void fraction at $t = \infty$, T_θ is the onset temperature for melting [K], and $C_{\chi 1}$, $C_{\chi 2}$ [K], and B are fitting constants. All fitting parameters for Eq. (9) are given in Table A.4 in Appendix A. Supplementary material.

It should be noted that h_r^* in Eq. (8) is dependent on the degree of impregnation, β, i.e. the resin layer thickness diminishes as the degree of impregnation increases,

$$h_r^* = h_{r,0}^* - \beta\left(\varphi_{fab} h_{fab}\right) \tag{10}$$

Where $h_{r,0}^*$ is the characteristic thickness of the resin volume, described by,

$$h_{r,0}^* = \varphi h_c \tag{11}$$

Naturally, degree of impregnation, β, varies as a function of the resin flow front position, l,

$$\beta = \frac{l}{\varphi_{fab} h_{fab}}, \quad l < L_1 \tag{12}$$

$$\beta = \frac{\varphi_1 h_{fab} + (l - \varphi_1 h_{fab})\varphi_2}{\varphi_{fab} h_{fab}}, \quad l \geq L_1 \tag{13}$$

where φ_1 and φ_2 are the inter-tow and intra-tow porosities, respectively (given in Table A.5 in Appendix A. Supplementary material [48,49,50,51,52]), and L_1 is the characteristic length of the inter-tow region [m] i.e. $\varphi_1 h_{fab}$.

The resin flow front position is based on Darcy's Law for flow in porous media [21]. In previous work [14,15], it has been shown that this material system undergoes dual-scale flow (i.e. macroscopic flow in the inter-tow region, and microscopic flow in the intra-tow region). As depicted in Fig. 1(c), the inter-tow and intra-tow flow regions can be modelled in series. Using this approach, 1D resin flow is described by,

$$\frac{dl}{dt} = \frac{4K_1}{\varphi_1 \eta} \frac{P_{app}}{l}, \quad l < L_1 \tag{14}$$

$$\frac{dl}{dt} = \frac{4K_2}{\varphi_2 \eta} \bullet \frac{K_1 P_{app}}{K_2 L_1 + K_1 (l - L_1)}, \quad l \geq L_1 \tag{15}$$

where K_1 and K_2 are the inter-tow and intra-tow permeabilities [m^2], respectively (given in Table A.5 in Appendix A. Supplementary material),η is the melt viscosity [Pa s], and P_{app} is the pressure applied by the vacuum bag i.e. compaction pressure [Pa].

The melt viscosity of the epoxy powder is described using the following chemorheological model [11],

$$\eta = \eta_{g0} \exp\left(\frac{-C_{\eta 1}[T - T_g]}{C_{\eta 2} + T - T_g} \right) \left(\frac{\alpha_g}{\alpha_g - \alpha} \right)^A \tag{16}$$

where η_{g0} is the viscosity of the uncured resin [Pa s], T_g is the glass transition temperature [K], α_g is the DoC at gelation, $C_{\eta 1}$, $C_{\eta 2}$ [K], and A are fitting constants. Parameter values for Eq. (16) can be found in Table A.6 in Appendix A. Supplementary material.

The cure kinetics are described using an existing model for epoxy powder [11],

$$\frac{d\alpha}{dt} = \frac{(k_{\alpha 1} + k_{\alpha 2} + k_{\alpha 3}\alpha^m)(1-\alpha)^n}{1 + \exp[C(\alpha - \alpha_c)]} \tag{17}$$

where $k_{\alpha 1}$, $k_{\alpha 2}$, and $k_{\alpha 3}$ are cure rate constants [s^{-1}] described by Arrhenius expressions, m and n are the reaction orders, C is a diffusion constant, and α_c is the temperature-dependent critical DoC, above which the reaction becomes diffusion-controlled.

The parameters for Eq. (17), along with the total enthalpy of the curing reaction, H_T, are given in Table A.7 in Appendix A. Supplementary material.

The DiBenedetto equation [53] was used to model the relationship between T_g and α, details of which can be found in Table A.8.

2.2. Numerical computation

Numerical computation of the relevant process models and material models was performed using two user-defined subroutines in Abaqus

FEA, namely, UMATHT and UEXPAN.

UMATHT allows for the definition of a material's thermal behaviour during a coupled temperature-displacement analysis. When the subroutine is called at a material calculation point, it solves the energy balance at that point using Newton's method for a given time increment and temperature increment. To assist in the definition of the material's thermal behaviour, UMATHT also allows for the use of solution-dependent state variables; the values of which are stored for each time increment.

The *heat equation*, described by Eq. (1), was used as the governing equation for energy balance in the laminate. To calculate the heat generation term in Eq. (1), it was necessary to define the DoC as a solution-dependent state variable and write a code within the UMATHT subroutine to solve the cure kinetic model (Eq. (17)); an ordinary differential equation (ODE). Using the same principle, it was also possible to solve the resin flow model (also an ODE) in addition to the sintering model and the chemorheological model. It was not possible, however, to update the element thickness (and, thereby, the laminate thickness) using UMATHT. Instead, the thickness change was updated via UEXPAN, a user subroutine that allows the user to define incremental thermal strains as a function of state variables.

Although many of the material properties were temperature-dependent, it was assumed that all material properties were constant within each time step and were evaluated at $T+\Delta T$ and $t+\Delta t$, i.e. material properties were not interpolated between the start and end of the increment. This simplified solving the energy balance; however, it also meant that the solution was sensitive to the increment size.

Another factor affecting the maximum allowable increment size was the numerical error associated with the methods being used to compute the cure kinetics and resin flow models. A fourth order Runge-Kutta method [54] was implemented in the subroutine to solve the ODEs. This method was numerically stable and was significantly more accurate than the first order Euler method previously developed for simulating this material system [14].

2.3. Virtual composite part development

Virtual composite parts were developed in Abaqus FEA using the in-built graphical user interface. Three geometries were investigated, as shown in Fig. 2: a 1D through-thickness section; a 3D quartered section of a flat laminate; and an axisymmetric section of a tapered wind turbine blade root.

The 1D geometry was designed to verify the numerical methods and compare simulated results against the experimental results described in [15] – the details of which will be elaborated on further in the next section. It was also used to test whether the 1D heat transfer assumption could be extended to the other two geometries i.e. to determine whether the use of 3D simulations was justified for those cases.

The 3D geometry represented a 420 mm × 420 mm × 100-ply laminate that was processed on a 10 mm steel tool in an oven. The material system was a stitched UD GF fabric with epoxy powder dispersed between each layer. A convective heat transfer coefficient (HTC) of 40 W/m^2 K was used for this geometry – the same value that was used in previous work for 1D simulations [14]. This part was developed to investigate the effects of in-plane heat transfer in anisotropic lay-ups. The symmetry of the flat laminate was used to reduce the geometry to a quarter section, thus reducing the computational cost of performing a simulation.

The tapered wind turbine blade root section was based on a 3D design supplied by industrial partners, however, the cylindrical geometry was reduced to an axisymmetric section to save on computational cost. It was assumed that the root section was made on a 10 mm thick steel tool in an oven with a uniform heat transfer coefficient of 40 W/m^2 K. It was also assumed that triaxial semi-preg (partially impregnated with epoxy powder) was used to fabricate the root section; triaxial glass-fibre (GF) fabrics are commonly used to resist load transfer between the airfoil section of the blade and the rotor hub [2].

In all cases, the geometries were constructed as 3D deformable solids, but were given arbitrary thicknesses in any unused directions, e.

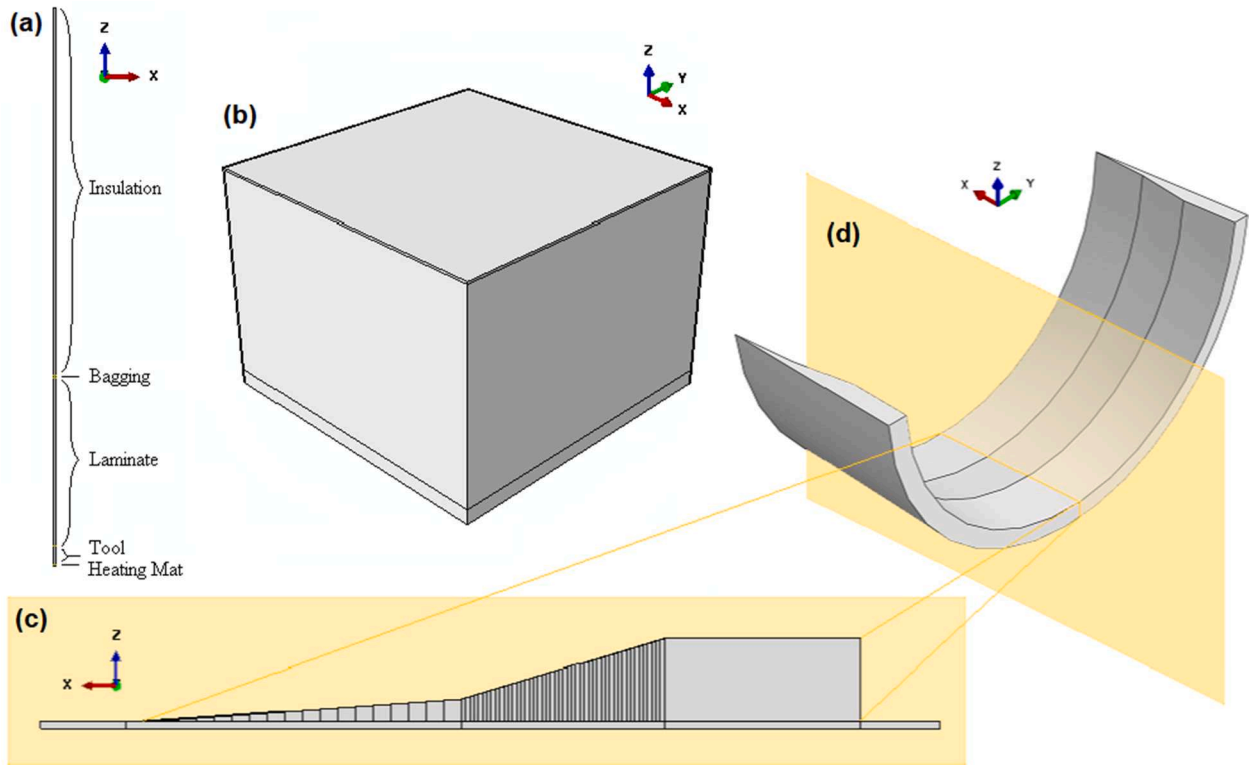

Fig. 2. Three types of geometry were created for analysis in Abaqus FEA: (a) a 1D through-thickness section; (b) a quartered section of a laminate on a flat tool; (c) an axisymmetric section of a tapered wind turbine blade root design (d), where the ply drops have been sectioned for meshing.

g. the 1D geometry was one element thick in the X and Y directions, while the asymmetric root geometry was one element thick in the Y direction. When meshing the parts, only structured meshing with hexahedral (brick) elements was used so that elements would represent individual plies or groups of plies e.g. for 100 plies, there may be 100 elements through the thickness (i.e. one ply per element), or 20 elements (5 plies per element). Partitioning was used to create the separate material sections for the laminate, insulation, bagging, etc., and to ensure that structured meshing with hexahedral elements was possible, see Fig. A.1 in Appendix A. Supplementary material. An 8-node thermally coupled brick, trilinear displacement and temperature (C3D8T) element was used for all simulations. Note that, due to difficulty with partitioning and meshing, the bagging layer was excluded from the axisymmetric root section geometry, which will be discussed further in the results and discussion section.

For each geometry, the bottom of the tool was given encastre mechanical boundary conditions, while any cut sections in the XZ or YZ planes were given mechanical symmetry boundary conditions. A transient coupled temperature-displacement analysis step was created for each geometry with the non-linear geometry option activated. Within this analysis step, thermal boundary conditions (i.e. specified temperature or forced convection) were applied where appropriate for each geometry. On any surface where the thermal boundary condition was not specified, Abaqus FEA assumed that the surface was perfectly insulated.

All remaining thermal properties used for the bagging and tool materials are given in Table A.9 [55]. In addition, mechanical properties were required by Abaqus FEA; the tool materials were given generic values for steel and aluminium, while the laminate and bagging materials were given arbitrary isotropic elastic values (1 GPa for Young's modulus and 0.3 for Poisson's ratio) to allow them to deform easily.

The initial conditions for each geometry are given in Table 1. For the 1D geometry, the initial conditions were matched to those used in Maguire et al. [15] for experimental validation. The initial conditions of the 3D geometry were matched to the 100-ply case study described in [14], which represents an idealised manufacturing scenario with no void formation or out-time effects (i.e. no vacuum leakage and a low initial DoC). The initial conditions of the axisymmetric root section geometry also used initial conditions for an idealised manufacturing scenario, however, ply thickness, degree of impregnation, and powder void fraction were adjusted to account for the use of triaxial semi-preg.

Where 1D simulations were performed for comparison to 3D simulations, the initial conditions of the 1D simulation were matched to that of the 3D simulations.

2.4. Brief description of experimental validation

Maguire et al. [15] performed a series of experiments to validate 1D simulations of the epoxy powder composite system. In relation to 3D heat transfer, the FEA model was validated against thermocouple data, which was provided by an industrial partner [18]. This section will provide a direct comparison of those experimental results and the simulated results from this present work.

In the case of 1D validation, three flat laminates were produced during these experiments (two with UD GF fabric, one with triaxial semi-preg), using vacuum-bag-only (VBO) processing. Thermocouple temperature plots for a 48-ply UD laminate are shown in Fig. 3, while the results for the other two test laminates can be found in Appendix A. Supplementary material (Figs. A.2 and A.3). As can be seen, the Abaqus FEA simulations produced accurate predictions of both the laminates' through-thickness temperature distribution and thickness change, producing similar results to the 1D finite difference code in [15].

In the case of 3D validation, a 96-ply laminate was produced by Finnegan et al. [18] using the same triaxial semi-preg system used in [15]. The 400 × 400 mm laminate was manufactured in an oven with thermocouples placed in the centre of the laminate and 100 mm from its edge. For the corresponding simulations, fitted convective boundary conditions were used as no information was available about the internal air flow of the oven.

Fig. 4 shows the percentage error between the simulations and thermocouple data for different locations in the laminate. As can be seen, the simulations once again show good accuracy, generally staying below 5% error. One exception is in the case of the curing stage; as no information was available about the storage conditions of the semi-preg, the initial degree of cure may have been higher than in the case of the pristine powder, which was characterised in [11] (i.e.) the simulations overpredicted the exotherm of the epoxy curing.

In terms of resin flow, the 1D experiments are considered sufficient validation as it has been observed that resin flow in the laminates is predominantly through-thickness (i.e. 1D), even in the case of oven heating where 3D heat transfer takes place. Nevertheless, further experimental validation of more complex parts is of interest for future work.

2.5. Convergence study

The run time for a simulation was dependent on the number of calculations performed and, therefore, the number of elements in the FEA mesh. Naturally, reducing the mesh density reduced the number of calculations, however, there was potential for a loss of accuracy with coarser meshes. As such, a convergence study on element size and time step size was performed for the 3D geometry; using 5 elements sizes between 10 and 30 mm, and 4 time steps sizes between 60 and 240 s. Figs. A.4 and A.5, in Appendix A. Supplementary material, show the simulation results for fine and coarse meshes, as well as large and small time step sizes. These comparisons show that the simulations were robust and showed little or no difference in either temperature change or thickness change.

While it was possible to increase the in-plane element size and time step size further, Fig. A.6 in Appendix A. Supplementary material shows that doing so would result in a relatively negligible decrease in simulation run time. For increased efficiency, it was possible to increase the element thickness to 10 times the ply thickness without a significant loss to the accuracy of the results (using a time step size of 240 s). This allowed for a simulation run time of under 4 min for the 3D geometry. Despite this, it was found that meshing composite part geometries with ply drops was easier when the element thickness was made equal to the ply thickness. As such, changing the in-plane mesh density was a more effective way to increase efficiency for more complex geometries, such as the tapered root section. If a better meshing strategy can be developed for more complex geometries (e.g. tapered sections with ply drops), using thicker elements would offer significant computational savings.

Table 1
Initial conditions for each simulated geometry.

Parameter [units]	1D geometry	3D geometry	Axisymmetric geometry
No. of plies	48	100	67
Cured ply thickness, h_c [m]	0.001	0.001	0.0013
Fibre volume fraction, V_f	0.45	0.5	0.5
Degree of impregnation, β	0.113	0.113	0.575
Powder void fraction, χ_0	0.503	0.485	0.175
Degree of cure, α	0.2	0.01	0.01
Applied pressure, P_{app} [Pa]	85×10^3	90×10^3	90×10^3
Ambient temperature, T [°C]	18	23	23

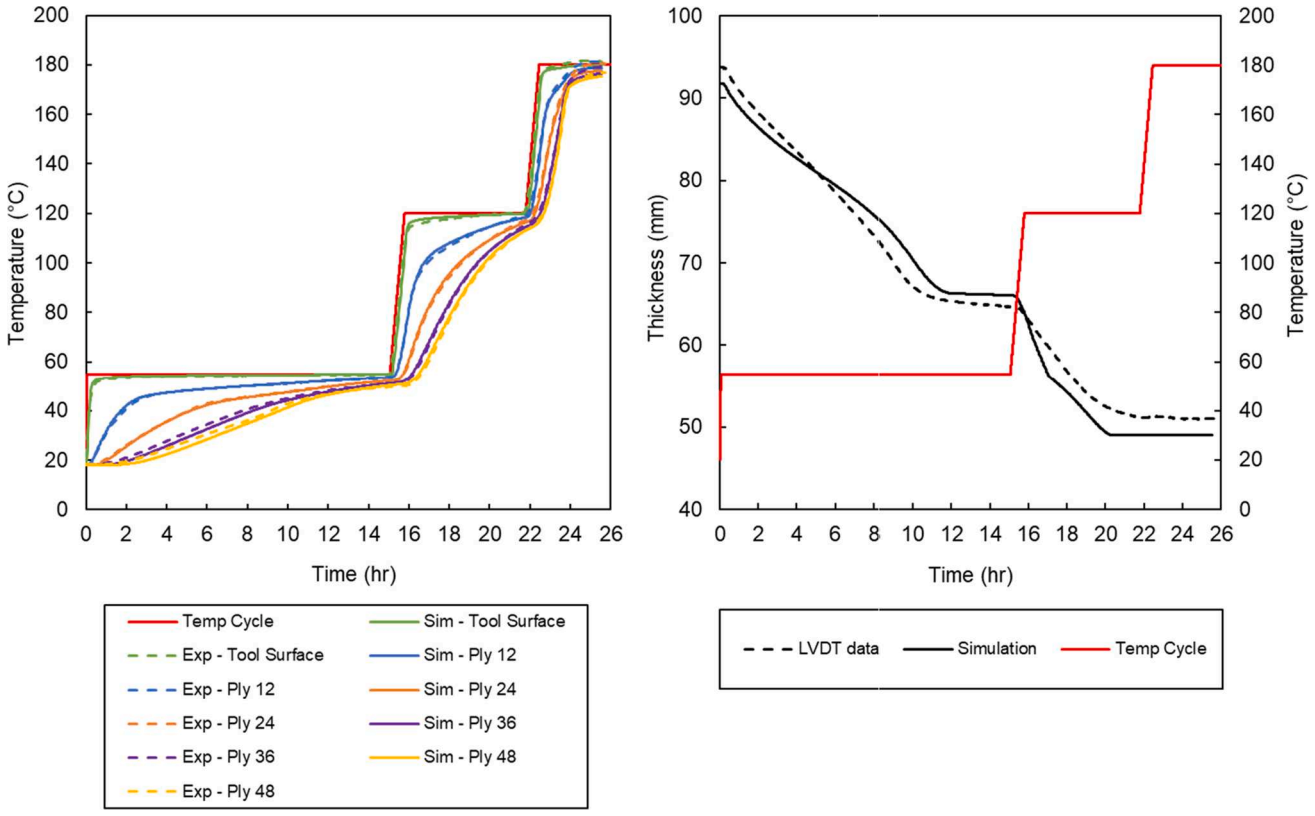

Fig. 3. Comparison of experimental data and simulation data for a 48-ply unidirectional GF/epoxy powder laminate manufactured on a heated tool with insulated boundaries: (left) comparison of thermocouple data and 1D simulated temperatures from Abaqus FEA; (right) comparison of LVDT data and the simulated laminate thickness change.

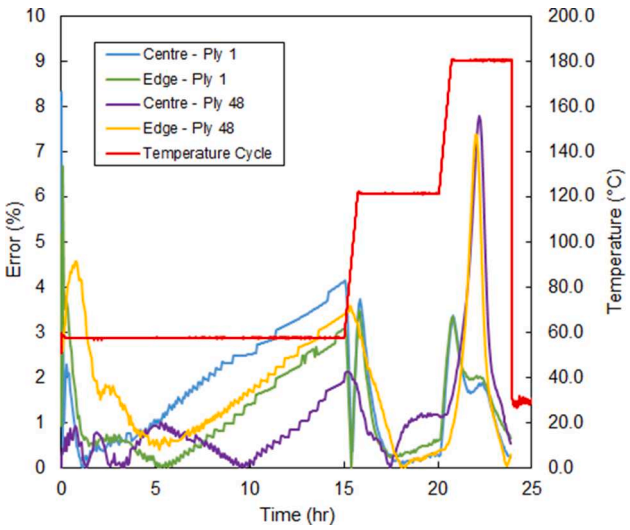

Fig. 4. Percentage error between thermocouple data and simulated temperatures for a 96-ply triaxial GF/epoxy powder laminate manufactured in an oven. "Edge" refers to thermocouples located 100 mm away from the edge of the 400 × 400 mm laminate.

3. Results and discussion

3.1. Process simulations of a generic thick-section laminate

3.1.1. General processing behavior

As previously mentioned, a 3D process simulation was performed on a generic 100-ply UD GF/epoxy-powder laminate for idealised initial conditions. As shown in Fig. 5, contour plots were produced for the drying stage, impregnation stage, and the cure stage of the temperature cycle. For each stage, a temperature plot is shown along with a second plot of the most important parameter at that stage of processing: powder void fraction is shown for the drying stage; degree of impregnation is shown for the impregnation stage; and degree of cure is shown at the cure stage. Note, Fig. A.7 in Appendix A. Supplementary material shows the temperature cycle that was used and also indicates the time step for each simulation result.

Fig. 5 also shows that the thickness of the laminate changed as the epoxy powder sintered and then impregnated the fabric. Thickness change was faster at the edges of the laminate than at its centre because of 3D thermal gradients. This outside-to-inside characteristic extended to each temperature-dependent process (i.e. sintering, impregnation, and curing). Centea et al. [56] have shown that this type of thermal gradient can result in high void contents when vacuum-bag-only (VBO) prepregs are used i.e. gas can be trapped in the centre of the laminate as gas pathways are sealed off at the laminate edges. Moreover, outside-to-inside curing can lead to the development of larger residual stresses in the cured laminate compared to inside-to-outside curing, as shown by Bogetti and Gillespie for a polyester resin system [1]. In the outside-to-inside case, the fully cured outer layers are put into compression, while the inner layers are put into tension as they cure and shrink. The timing of the development of cure gradients and thermal gradients is critical. If the gradients develop while the inner layers undergo gelation, then warpage, voids, and/or micro-cracking can occur due to the weak mechanical properties of the resin [57]. As such, for the case presented here, the primary concerns were gradients in temperature and DoC during the cure stage – differences of 40 °C and 0.5 (50%) can be seen in Fig. 5(e) and (f), respectively. Modelling gas evacuation and residual stress development were outside the scope of current research, however, methods to reduce thermal gradients and cure gradients will discussed in

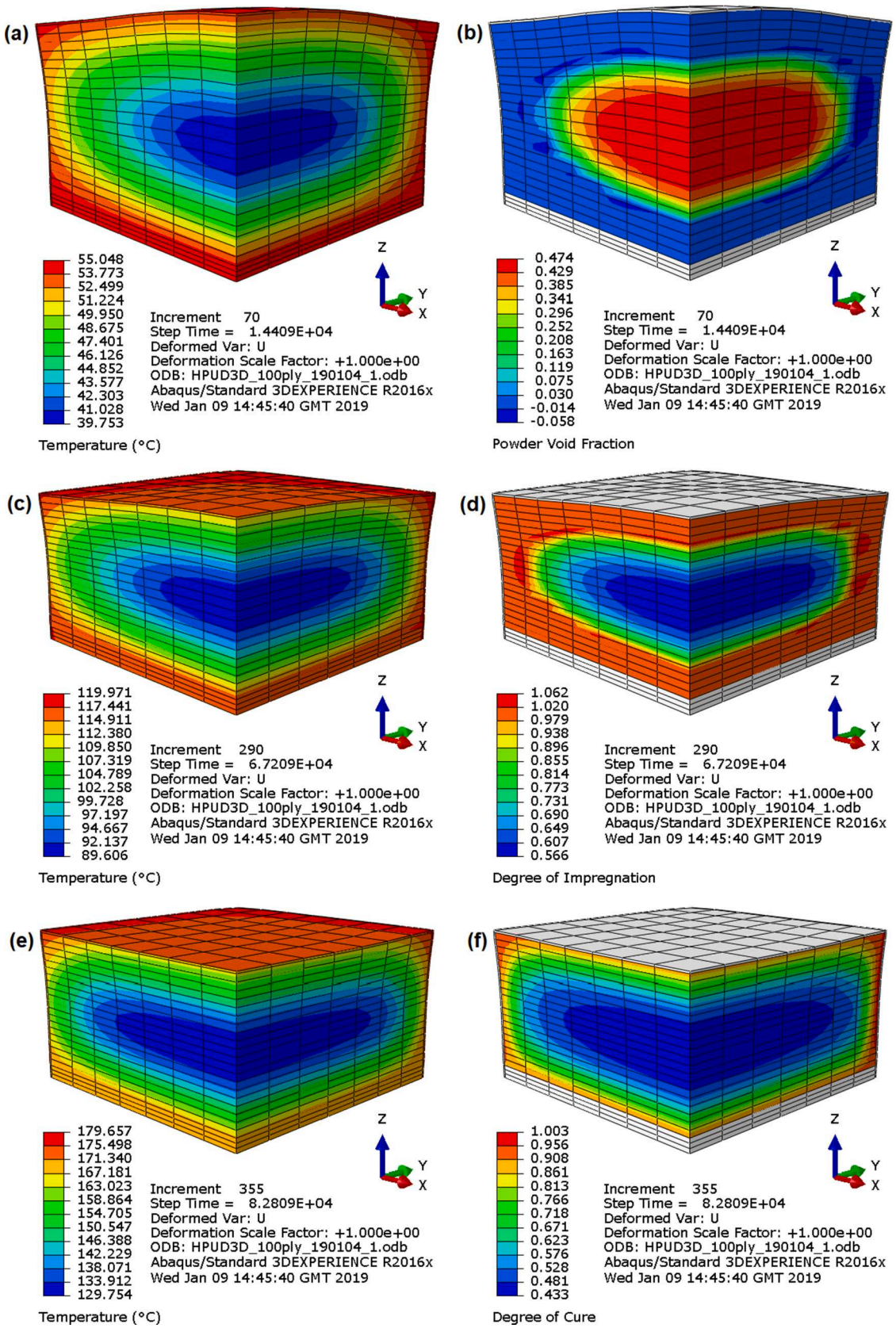

Fig. 5. Contour plots of the 100-ply UD GF/epoxy laminate during the processing. (a) Temperature and (b) powder void fraction during the drying stage (4 hr into the cycle). Higher temperatures at the edges resulted in faster sintering and uneven thickness change. (c) Temperature and (d) degree of impregnation during the impregnation stage (18.67 hr into the cycle). Faster impregnation at the edges could impede gas evacuation. (e) Temperature and (f) degree of cure during the curing stage (i.e. 23 h into the cycle). Peaks in the thermal and cure gradients coincided with gelation. The laminate exhibited outside-to-inside curing which created a fully cured shell around the partially cured core.

later sections (e.g. a modified temperature cycle [14]).

3.1.2. Effects of in-plane heat conduction

The power of 1D simulations comes from their computing efficiency, however, in most practical cases, thick-section composites will be subject to 3D heat transfer. This brings into question the validity of using 1D simulations to optimise the temperature cycle for thick sections. Often, a key factor is the accuracy of the 1D simulation in predicting the processing conditions at the centre of the laminate. As can be seen in Fig. 5, the centre of a thick-section epoxy powder laminate will typically be the last location to complete impregnation and curing. As has been shown in the literature, whether the 1D simulations can accurately predict processing conditions at the centre of a laminate depends on the ratio of laminate thickness to in-plane dimensions [58], and the ratio of anisotropy with respect to the thermal conductivities [31].

Due to the relatively small difference between longitudinal and transverse thermal conductivity of UD GF/epoxy laminates, Oh and Lee [29] showed that heat transfer was almost symmetric in the XZ and YZ planes. Fig. 5(a) and (c) show that this was not necessarily the case for powder-based laminates; at the beginning of the process cycle, the low thermal conductivity of the powder meant that heat transfer along the fibres was dominant. For example, at 4 hr, the laminate's through-thickness thermal conductivity, κ_{ZZ}, was between 0.127 and 0.2 W/m·K, whereas the thermal conductivity in the direction of the fibres, κ_{XX}, ranged between 0.69 and 0.737 W/m·K. This resulted in a ratio of anisotropy (κ_{XX}/κ_{ZZ}) as high as 5.55. In comparison, at 21 hr (i.e. the end of the impregnation stage) the ratio of anisotropy was reduced to 2.68. Effectively, as the epoxy sintered and began to impregnate the laminate, both the through-thickness and transverse thermal conductivities increased and the longitudinal component became less influential. This behavior was reflected in the comparison between the 1D model and the 3D model, shown in Fig. 6. As can be seen, there was greater discrepancy between the two models when the ratio of anisotropy was greater (i.e. earlier in the temperature cycle). Nevertheless, the results of Fig. 6 show that 1D simulations offer an accurate prediction of process conditions at the in-plane centre of the 3D geometry for a UD GF/epoxy material system; being within the same margin of error as the 3D simulation when compared to the experimental data.

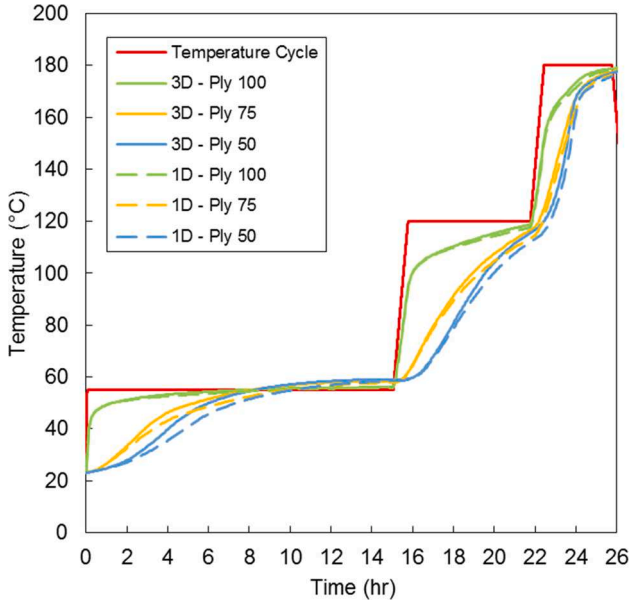

Fig. 6. Comparison of 1D and 3D temperature predictions in a 100-ply UD glass-fibre laminate. The mismatch between the results was more prevalent when the epoxy was in powder form and the ratio of anisotropy of thermal conductivities was greater.

With regards to the ratio of anisotropy for thermal conductivities, it was interesting to consider the influence of edge effects for carbon-fibre (CF) laminates. A repeat simulation was performed for the 3D quartered geometry using the CF material properties/parameters given in Tables A.3 and A.5 in Appendix A. Supplementary material. All other properties/parameters were kept the same as the previous simulation; including the fibre direction which was parallel to the X axis.

As shown in Fig. 7, the greater thermal conductivity of the carbon fibres resulted in asymmetric in-plane heat transfer. When comparing the temperatures at the centre of the laminate to a 1D simulation, it was clear that the difference between the models was significantly greater than for the GF laminate. Due to in-plane heat transfer, the entire laminate also approached the programmed oven temperature much faster than the GF laminates. This resulted in the powder sintering at an increased rate, which would have an effect on moisture desorption and gas evacuation.

Additionally, it was noted that the laminate did not reach full impregnation for the normal temperature cycle due to the lower permeability of CF tows (see Fig. 8 – impregnation is represented by thickness change during the impregnation stage). Using the modified temperature cycle developed by Maguire et al. [15], it was possible to achieve full impregnation for the laminate due to the shortened drying stage and extended impregnation stage. Note, this temperature cycle was originally developed to reduce thermal gradients and cure gradients during gelation within the laminate, however, this result showed that there were additional, unforeseen benefits to this cycle.

Simulations were performed for triaxial fabrics also (both GF and CF). The ratios of anisotropy for each simulated laminate are given in Table 2; in each case, a range was given because the ratios varied over the duration of the temperature cycle as a function of the material state i.e. temperature, powder void fraction, degree of impregnation, etc. As expected, the ratio of anisotropy was significantly greater for the carbon fibre laminates.

Overall, it was clear from the results that part dimensions and thermal conductivity must be carefully considered before using 1D simulations to optimise a temperature cycle.

3.2. Process simulations of a wind turbine blade root section

3.2.1. Standard temperature cycle

Geometrical complexity plays an additional role in determining which kind of process simulation should be performed for a structure; 1D, 2D, or 3D. For the root section geometry, shown in Fig. 2(c) and (d), the thickness tapers along the blade axis (in the X direction) but is unchanged in the tangential direction (about the X axis). As such, it was assumed that in-plane heat transfer was negligible in the tangential direction, and an axisymmetric cross-section (in the XZ plane) was created using triaxial semi-preg, as previously described.

The standard temperature cycle was used to perform initial simulations. It should be noted that, due to difficulties with meshing, the bagging layer was excluded from the axisymmetric root section simulations. To assess the effects of this exclusion, 1D simulations were performed, with and without a bagging layer, at the thickest section of the laminate. The results showed some minor discrepancies in temperature prediction, particularly in the topmost plies near the bagging surface (see Fig. A.8 in Appendix A. Supplementary material). Nevertheless, for demonstration purposes, the axisymmetric results can be considered a good approximation of actual processing conditions.

Contour plots of temperature and DoC are shown in Fig. 9 for the axisymmetric root section manufactured using the standard temperature cycle. While tooling was included in the simulations, it has been removed from view in the contour plots. Furthermore, the detail of the meshing has been removed from the contours to allow greater image clarity.

While the temperature and DoC remained relatively uniform in the thinner end of the root, large thermal gradients and cure gradients

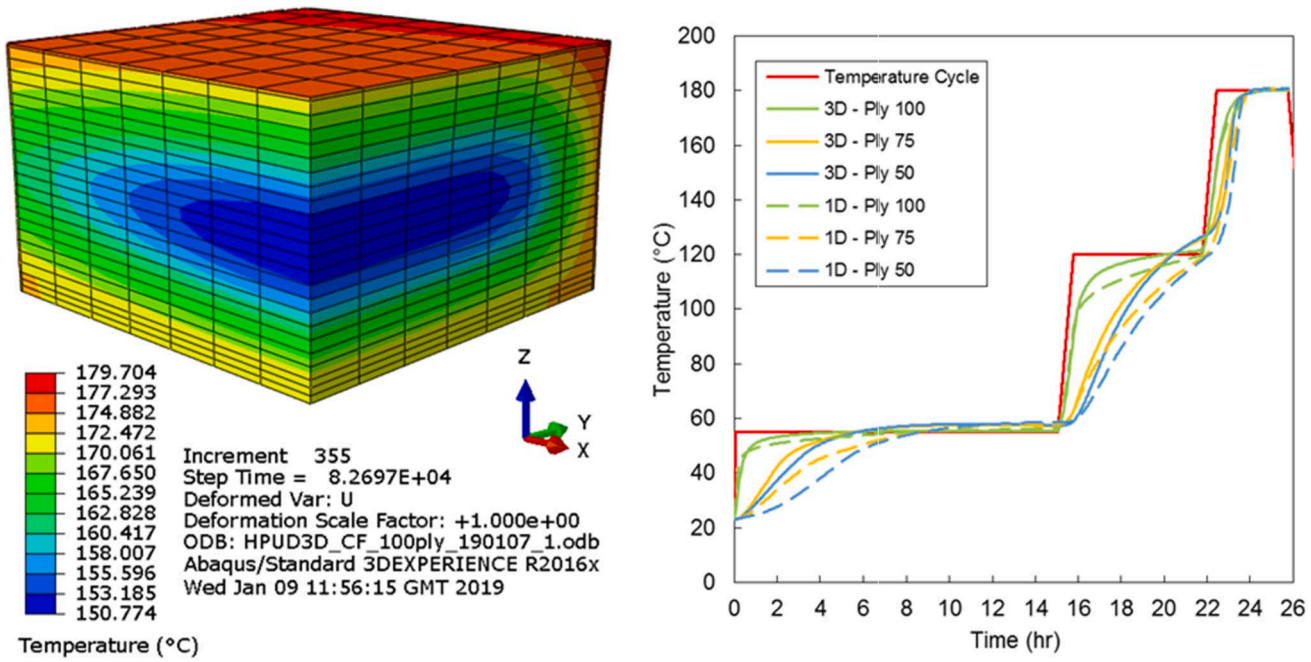

Fig. 7. Temperature predictions for a 100-ply UD CF/epoxy-powder laminate: (left) shown at 23 hr, the temperature gradients in the XZ and YZ planes were asymmetric due to the higher thermal conductivity in the longitudinal (X) direction (i.e. parallel to the fibre direction); (right) there was a significant difference between the 1D and 3D results for temperature prediction at the centre of the laminate.

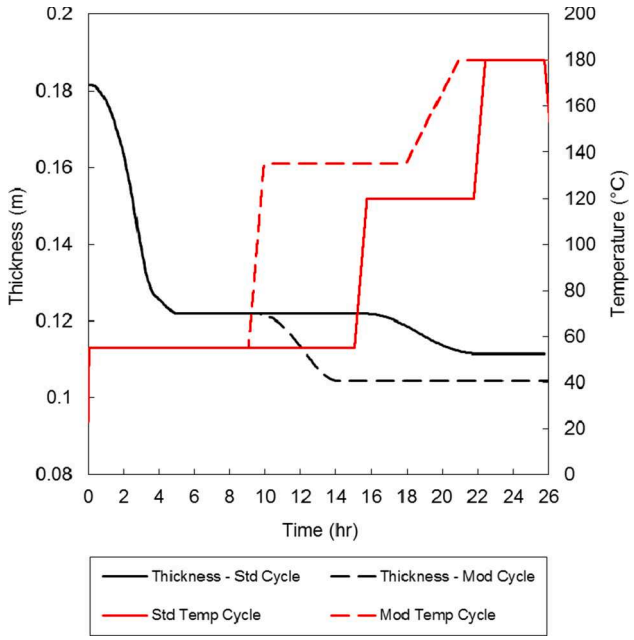

Fig. 8. Simulated thickness change for the 100-ply UD CF laminate using the standard temperature cycle and a modified temperature cycle from [15]. The laminate failed to fully impregnate for the standard cycle. By beginning the impregnation stage earlier, the modified cycle achieved sufficiently low viscosities to impregnate the carbon fibre tows.

developed in the thicker end of the root. Similar to the 3D geometry, it can be seen that this resulted in an outside-to-inside curing pattern. It was expected that the modified temperature cycle (previously shown in Fig. 8), would alleviate the gradients in the thicker region, however, it was found that temperature cycle needed to be adjusted further for the semi-preg material format. For an iterative task such as this, the axisymmetric simulation was relatively inefficient (i.e. run time of 677 s) compared to 1D simulations (run time of 87 s or less). To test whether a 1D approximation would be valid for this case, the 1D results were compared with the temperature distribution of the axisymmetric simulation at X = 185 mm i.e. the point least affected by in-plane heat transfer. Little variation was found between the results, suggesting the 1D approximation was valid; see Fig. A.9 in Appendix A. Supplementary material. Consequently, 1D simulations were used for iterative modification of the temperature cycle.

Table 2
Ratio of anisotropy for the various laminates that were simulated.

Material type	Ratio of anisotropy*
Uni-directional GF	2.08–5.55
Triaxial GF	1.80–4.42
Uni-directional CF	5.54–35.79
Triaxial CF	4.44–27.10

*Ratio of anisotropy between the longitudinal thermal conductivity and the through-thickness thermal conductivity.

3.2.2. *Modified temperature cycle*

The modified temperature cycle for this case was as follows:

- Drying stage: Ramp to 55 °C and hold for 540 min
- Impregnation stage: Ramp to 120 °C at 1.0 °C/min and hold for 480 min
- Cure stage: Ramp to 180 °C at 0.25 °C/min and hold for 300 min

As described previously by Maguire et al. [15], the objective of modifying the temperature cycle was to minimise the thermal gradients and cure gradients in the laminate as it was undergoing gelation. The motivation for this was that the elastic modulus of thermosetting composites begins to develop during gelation, acting as starting point for residual stress development [57]. Therefore, to avoid trapping large residual stresses in the laminate, it is important to minimise these gradients during the cure stage, particularly during gelation when the nascent crosslinking network can be damaged.

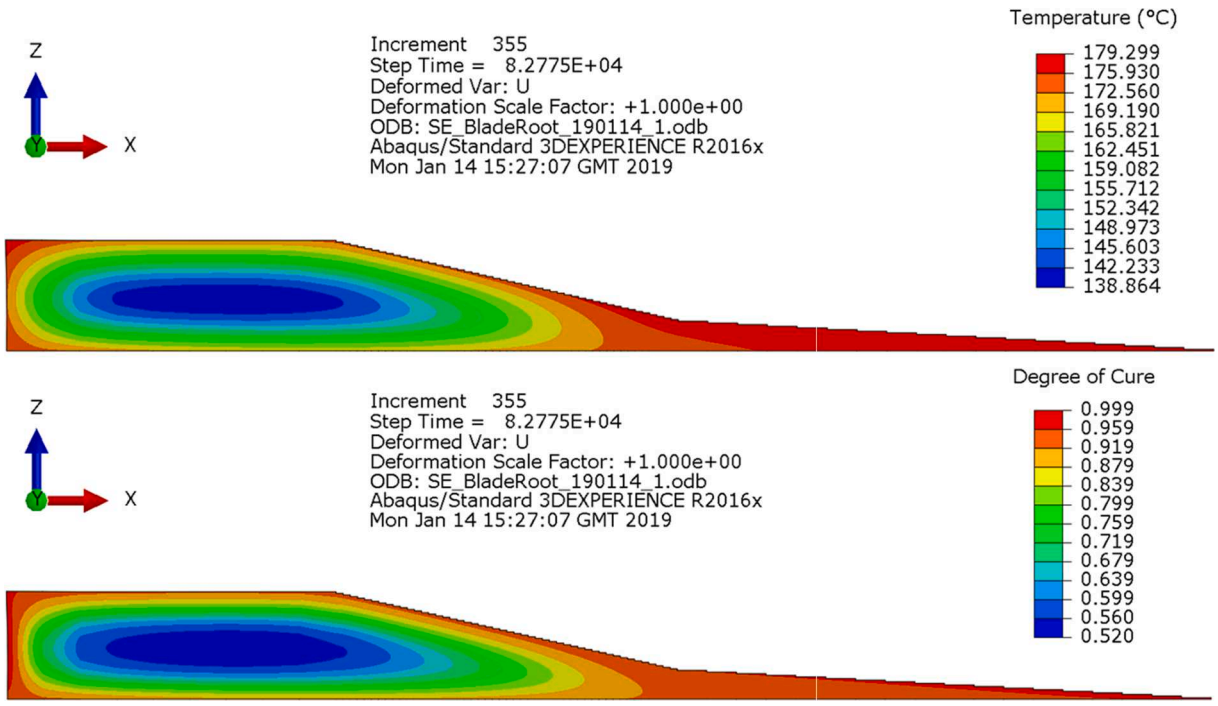

Fig. 9. Contour plots of temperature (top) and DoC (bottom) along the XZ plane of a simulated root section. The plots show conditions during the cure stage of a standard temperature cycle (i.e. 23 hr into the cycle). Large thermal gradients and cure gradients form in the thicker end of the root.

As can be seen in Fig. 10, the new temperature cycle resulted in relatively small differences in temperature and DoC between the outside and centre of the laminate during gelation (less than 5 °C and 0.1 (10%), respectively). This was a significant reduction compared to the results for the standard cycle (approx. 40 °C and 0.4 (40%)). Note that the values for Fig. 10 were taken 185 mm from the end of the blade root (in the X direction).

In addition to a modified temperature cycle, Maguire et al. [15] investigated the use of heated tooling and flexible heating mats as an alternative heating method to oven heating. It was proposed that this method could potentially be more cost-effective for manufacturing thick parts than oven heating. Assuming that one-sided heating was sufficient to process the thinner end of the tapered blade root, it was considered worthwhile to re-explore this concept here.

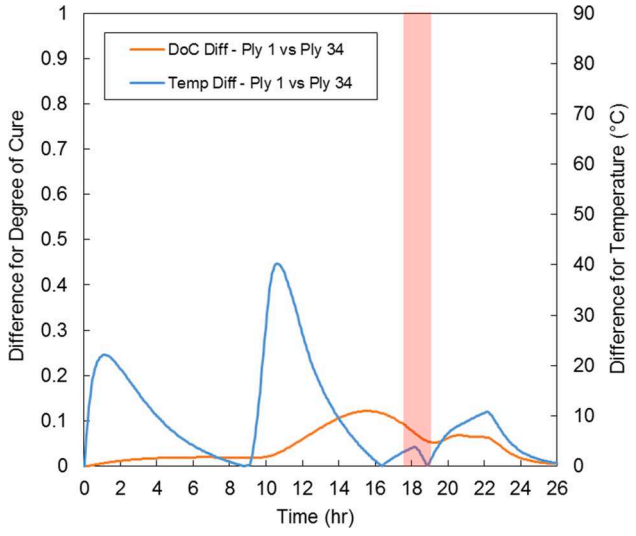

Fig. 10. The temperature difference and DoC difference between the outside of the section (Ply 1) and the centre (Ply 34) for the modified temperature cycle. The red shaded area represents the period of gelation within the section.

The modified temperature cycle for the root section was implemented using specified temperature boundary conditions on both the underside of the steel tool and the top surface of the thickest part of the root, as shown in Fig. 11. Insulated boundary conditions were assumed for all other surfaces.

Fig. 11 show the effects of using heated tooling and flexible heating mats. The thermal gradients and cure gradients were lower during gelation than for oven heating; differences in temperature and DoC of approx. 7 °C and 0.07 (7%), respectively. The abrupt transition from two-sided heating to one-sided heating creates some localised gradients; however, these were also relatively low. To mitigate this effect, the length of the flexible heating mat could be increased to heat more of the top surface, or heating mats with zonal control could be employed. This concept may be particularly useful for parts that are too large to fit into a conventional oven, such as blade spars. As multiple mats would be in use, the temperature cycle could be controlled on a zone-by-zone basis to minimise in-plane gradients and energy usage.

Although the root section of turbine blades are typically made from glass-fibre composites, carbon fibre composites are of interest for very large wind turbine blades and tidal turbine blades [59]. As such, it was a worthwhile exercise once again to consider how the ratio of anisotropy would affect processing. For this reason, a simulation was performed with triaxial CF fabric using the modified temperature cycle (the dimensions of the geometry were not altered). Fig. 12 shows that the temperature difference in the thickest section of the part has been reduced to an average of approximately 1 °C during gelation. This was due to a combination of the modified temperature cycle, the specified boundary conditions and the presence of carbon fibres, which allowed larger amounts of in-plane heat transfer, particularly in the X direction.

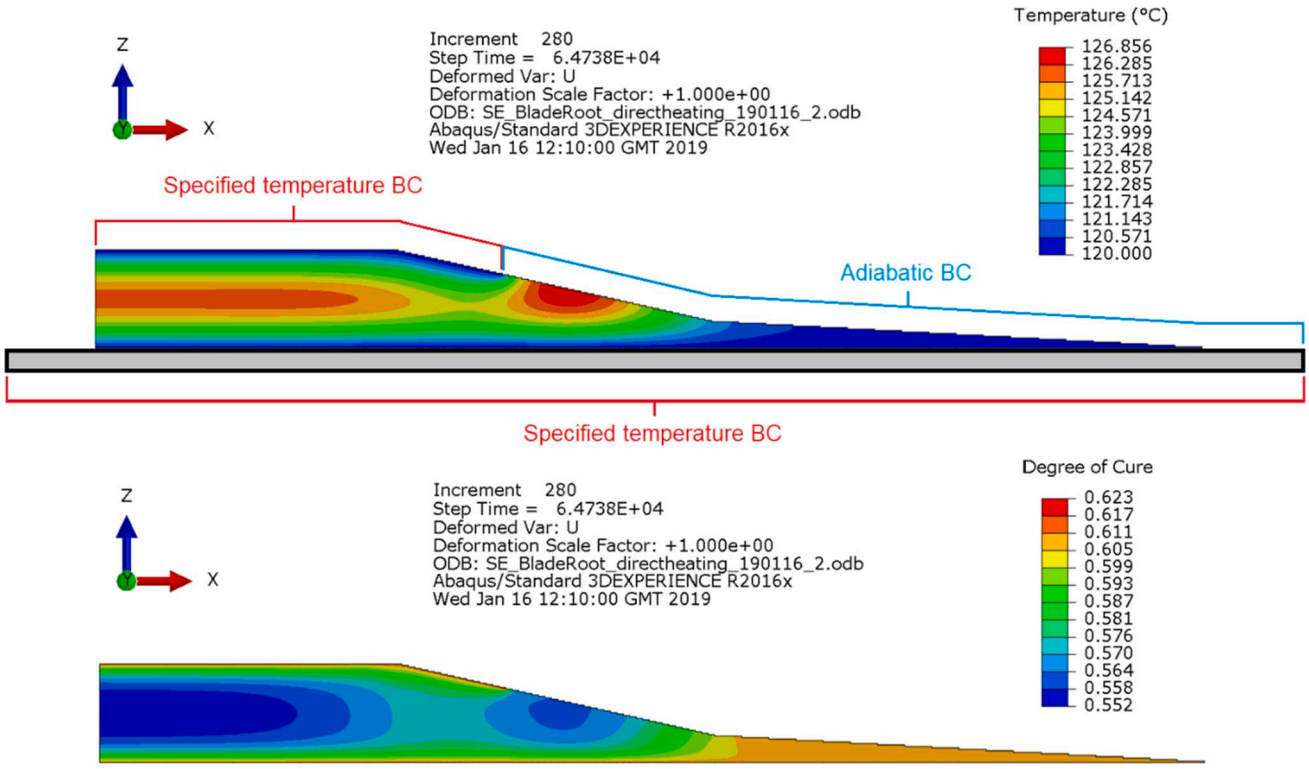

Fig. 11. Contour plots of temperature (top) and DoC (bottom) along the XZ plane of a simulated root section. The plots show conditions 18 h into the modified temperature cycle when the epoxy was undergoing gelation. Note that illustrations have been added to the top contour plot to show how the thermal boundary conditions (BCs) were applied.

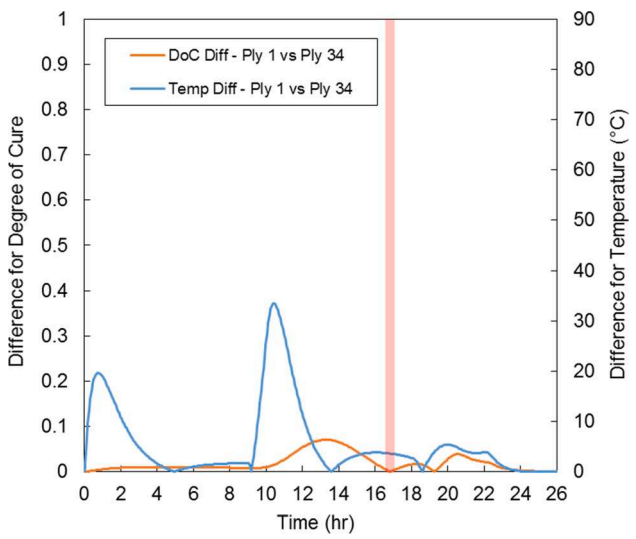

Fig. 12. The temperature difference and DoC difference between the outside of the blade root (Ply 1) and the centre (Ply 34) when triaxial CF fabric was used. The period of gelation in the laminate was very short because there was little or no difference in the DoC (through-thickness) at that point in time. The data was taken 185 mm from the end of the section.

4. Conclusions

Numerical methods for performing 1D and 3D process simulations have been presented. The simulations focussed on the processing of thick-section laminates via powder-based vacuum-bag-only (VBO) materials. The simulations were performed using coupled temperature-displacement analysis tools in Abaqus FEA along with user-defined subroutines that described the resin flow, powder sintering, and cure kinetics within the composite material. Three main geometries were considered; a 1D through-thickness geometry, a 3D quartered section of a flat laminate, and an axisymmetric section of a cylindrical wind turbine blade root. Simulations for the 1D geometry were compared against experimental data from previously published work. A convergence study showed that the numerical methods were robust for varying time step sizes and element sizes. In this sense, it can be concluded that commercial software was two orders of magnitude more efficient in comparison to the finite difference code previously developed for this material system. Nevertheless, implementation of the process models in the user-defined subroutines was a challenging process and benefitted from the previous development of the finite difference code.

The effects of in-plane heat transfer were investigated using the 3D quartered section. It was found that heat transfer in the fibre direction had a greater influence in the first two stages of the temperature cycle; the powder sintering stage and the impregnation stage. This was due to the low thermal conductivity of the powder and dry fabric, which inhibited through-thickness heat transfer. As a result, all the critical processes, such as powder sintering, fabric impregnation, and curing, occurred in an outside-to-inside pattern.

The mismatch between in-plane and through-thickness heat transfer became more severe when carbon fibres were considered. In terms of thermal conductivity, it was shown that, depending on the stage of the temperature cycle, the ratio of anisotropy for carbon-fibre fabrics was up to an order of magnitude greater than for glass-fibre fabrics. It was also shown that fabric impregnation was significantly slower for carbon-fibre fabrics, and a modified cycle was required to achieve full impregnation with the epoxy powder. Due to the influence of in-plane heat conduction, the validity of a 1D (through-thickness) heat transfer assumption was tested for the 3D geometry. It was shown that the discrepancies between 1D and 3D simulations were significantly greater for carbon-fibre fabrics than for glass-fibre fabrics due to the greater ratio of anisotropy. As a result, the 1D assumption may be limited for some practical cases of thick-section carbon-fibre laminates because the in-

plane dimensions must be significantly larger than the laminate thickness.

Additionally, the choice of 1D or 3D simulation was considered for a turbine blade root geometry, which was tapered via ply-drops. As the cross-section was uniform in the tangential direction, an axisymmetric simulation was implemented. Nevertheless, it was shown that 1D simulations could be used as well to determine key processing criteria, such as the completion of impregnation and cure. Consequently, 1D simulations were used to modify the temperature cycle for that geometry and VBO semi-preg format, while axisymmetric 3D simulations were used to acquire more complete process information for the overall part.

An alternative heating method, previously developed by Maguire et al. [15], was re-investigated for the tapered root section. This method used heated tooling and heating mats to apply two-sided heating locally to the thickest section of the root while the thinner part of geometry was heated on one side only. It was shown that the blade root could be fully processed using this method and, compared to conventional ovens, this arrangement could offer more energy efficient heating of large thick-section parts.

Finally, the implications of using carbon-fibre was considered for the turbine blade root. It was shown that, due to in-plane heat conduction, the through-thickness temperature and DoC differences were relatively small. Although turbine blade roots are typically made using glass-fibre fabrics, unidirectional carbon-fibre is increasingly being used to produce spar caps for very large turbine blades (>60 m in length). As such, faster in-plane heat transfer may represent an added benefit of using carbon fibres in this application.

CRediT authorship contribution statement

James M. Maguire: Methodology, Software, Validation, Formal analysis, Investigation, Writing – original draft, Project administration, Funding acquisition. **Nathan D. Sharp:** Methodology, Software, Supervision. **R. Byron Pipes:** Resources, Writing – review & editing, Supervision, Project administration. **Conchúr M. Ó Brádaigh:** Resources, Writing – review & editing, Supervision, Project administration, Funding acquisition.

Declaration of Competing Interest

The authors declare that they have no known competing financial interests or personal relationships that could have appeared to influence the work reported in this paper.

Data availability

The data that has been used is confidential.

Acknowledgements

The initial stages of this work were carried out at the Composites Manufacturing and Simulation Center at Purdue University, which was funded by the John Moyes Lessells Travel Scholarship from the Royal Society of Edinburgh. The authors acknowledge additional financial support from the Institute of Materials and Processes at the University of Edinburgh and POWDERBLADE, "Commercialisation of Advanced Composite Material Technology: Carbon-Glass Hybrid in Powder Epoxy for Large Wind Turbine Blades", funded under: European Union Horizon 2020, Fast Track to Innovation Pilot, Grant No. 730747. We also acknowledge the support of industrial partners Suzlon Energy Limited (NL Branch), Johns Manville, and ÉireComposites Teo.

Appendix A. Supplementary material

Supplementary data to this article can be found online at https://doi.org/10.1016/j.compositesa.2022.107073.

References

[1] Bogetti TA, Gillespie JW. Process-induced stress and deformation in thick-section thermoset composite laminates. J Compos Mater 1992;26:626–60. https://doi.org/10.1177/002199839202600502.
[2] Wieland B, Ropte S. Process modeling of composite materials for wind-turbine rotor blades: experiments and numerical modeling. Materials (Basel) 2017;10:1157–69. https://doi.org/10.3390/ma10101157.
[3] Hardis R, Jessop JLP, Peters FE, Kessler MR. Cure kinetics characterization and monitoring of an epoxy resin using DSC, Raman spectroscopy, and DEA. Compos Part A Appl Sci Manuf 2013;49:100–8. https://doi.org/10.1016/j.compositesa.2013.01.021.
[4] Harper P, Hallett S, Fleming A, Dawson M. 9 – Advanced fibre-reinforced composites for marine renewable energy devices. Mar Appl Adv Fibre-Reinforced Compos, Woodhead Publishing 2016:217–32. https://doi.org/10.1016/B978-1-78242-250-1.00009-0.
[5] Hsiao K-T, Heider D. 10 – Vacuum assisted resin transfer molding (VARTM) in polymer matrix composites. Manuf Tech Polym Matrix Compos, Woodhead Publishing Limited 2012;10:310–47. https://doi.org/10.1533/9780857096258.3.310.
[6] Nijssen R, de Winkel GD. 5 – developments in materials for offshore wind turbine blades. Offshore Wind Farms, Woodhead Publishing 2016:85–104. https://doi.org/10.1016/B978-0-08-100779-2.00005-2.
[7] Murray RE, Jenne S, Snowberg D, Berry D, Cousins D. Techno-economic analysis of a megawatt-scale thermoplastic resin wind turbine blade. Renew Energy 2019;131:111–9. https://doi.org/10.1016/j.renene.2018.07.032.
[8] Centea T, Grunenfelder LK, Nutt SR. A review of out-of-autoclave prepregs – material properties, process phenomena, and manufacturing considerations. Compos Part A Appl Sci Manuf 2015;70:132–54. https://doi.org/10.1016/j.compositesa.2014.09.029.
[9] Hollaway LC. 10 – High performance fibre-reinforced composites for sustainable energy applications. High Perform Text Appl, Woodhead Publishing 2014;10:366–417. https://doi.org/10.1533/9780857099075.366.
[10] Radanitsch J. Multi-layered carbon stacks for large wind turbine blades. Proc CAMX 2014, Orlando, FL, USA; 2014.
[11] Maguire JM, Nayak K, ÓBrádaigh CM. Characterisation of epoxy powders for processing thick-section composite structures. Mater Des 2018;139:112–21. https://doi.org/10.1016/J.MATDES.2017.10.068.
[12] Gardiner G. Big parts? Big tooling breakthrough. Compos World; 2012.
[13] Ó Brádaigh CM, Doyle A, Doyle D, Feerick PJ. Electrically-heated ceramic composite tooling for out-of-autoclave manufacturing of large composite structures. SAMPE J; 2011. p. 47.
[14] Maguire JM, Simacek P, Advani SG, Ó Brádaigh CM. Novel epoxy powder for manufacturing thick-section composite parts under vacuum-bag-only conditions. Part I: Through-thickness process modelling. Compos A Appl Sci Manuf 2020;136:105969. https://doi.org/10.1016/j.compositesa:2020.105969.
[15] Maguire JM, Nayak K, Ó Brádaigh CM. Novel epoxy powder for manufacturing thick-section composite parts under vacuum-bag-only conditions. Part II: Experimental validation and process investigations. Compos A Appl Sci Manuf 2020;136:105970. https://doi.org/10.1016/j.compositesa:2020.105970.
[16] Robert C, Pecur T, Maguire JM, Lafferty AD, McCarthy ED, Ó Brádaigh CM. A novel powder-epoxy towpregging line for wind and tidal turbine blades. Compos Part B Eng 2020;203:108443.
[17] Floreani C, Cuthill F, Steynor J, Maguire JM, McCarthy ED, Niessink MJ, et al. Testing of a 6 m hybrid glass/carbon fibre powder epoxy composite wind blade demonstrator. SAMPE J; 2021 May/June:6–14.
[18] Finnegan W, Allen R, Glennon C, Maguire J, Flanagan M, Flanagan T. Manufacture of high-performance tidal turbine blades using advanced composite manufacturing technologies. Appl Compos Mater 2021;28(6):2061–86. https://doi.org/10.1007/s10443-021-09967-y.
[19] Centea T, Hubert P. Modelling the effect of material properties and process parameters on tow impregnation in out-of-autoclave prepregs. Compos Part A Appl Sci Manuf 2012;43:1505–13. https://doi.org/10.1016/j.compositesa.2012.03.028.
[20] Cender TA, Simacek P, Advani SG. Resin film impregnation in fabric prepregs with dual length scale permeability. Compos Part A Appl Sci Manuf 2013;53:118–28. https://doi.org/10.1016/j.compositesa.2013.05.013.
[21] Darcy H. Les fontaines publiques de la ville de Dijon. Paris, France; 1856.
[22] Loos AC, Springer GS. Curing of epoxy matrix composites. J Compos Mater 1983;17:135–69. https://doi.org/10.1177/002199838301700204.
[23] Martinez GM. Fast cures for thick laminated organic matrix composites. Chem Eng Sci 1990;46:439–50. https://doi.org/10.1016/0009-2509(91)80005-J.
[24] Twardowski TE, Lin SE, Geil PH. Curing in thick composite laminates: experiment and simulation. J Compos Mater 1993;27:216–50. https://doi.org/10.1177/002199839302700301.
[25] Young W-B. Compacting pressure and cure cycle for processing of thick composite laminates. Compos Sci Technol 1995;54:299–306. https://doi.org/10.1016/0266-3538(95)00067-4.
[26] Bogetti TA, Gillespie JW. Two-dimensional cure simulation of thick thermosetting composites. J Compos Mater 1991;25:239–73. https://doi.org/10.1177/002199839102500302.
[27] Yi S, Hilton HH, Ahmad MF. A finite element approach for cure simulation of thermosetting matrix composites. Comput Struct 1997;64:383–8. https://doi.org/10.1016/S0045-7949(96)00156-3.
[28] Joshi SC, Liu XL, Lam YC. A numerical approach to the modeling of polymer curing in fibre-reinforced composites. Compos Sci Technol 1999;59:1003–13. https://doi.org/10.1016/S0266-3538(98)00138-9.

[29] Oh JH, Lee DG. Cure cycle for thick glass/epoxy composite laminates. J Compos Mater 2002;36:19–45. https://doi.org/10.1177/0021998302036001300.
[30] Costa VAF, Sousa ACM. Modeling of flow and thermo-kinetics during the cure of thick laminated composites. Int J Therm Sci 2003;42:15–22. https://doi.org/10.1016/S1290-0729(02)00003-0.
[31] Yan X. Finite element simulation of cure of thick composite: formulations and validation verification. J Reinf Plast Compos 2008;27:339–55. https://doi.org/10.1177/0731684407083007.
[32] Park HC, Goo NS, Min KJ, Yoon KJ. Three-dimensional cure simulation of composite structures by the finite element method. Compos Struct 2003;62:51–7. https://doi.org/10.1016/S0263-8223(03)00083-7.
[33] Zimmermann K, Van Den Broucke B. Assessment of process-induced deformations and stresses in ultra thick laminates using isoparametric 3D elements. J Reinf Plast Compos 2012;31:163–78. https://doi.org/10.1177/0731684411433315.
[34] Sorrentino L, Polini W, Bellini C. To design the cure process of thick composite parts: experimental and numerical results. Adv Compos Mater 2014;23:225–38. https://doi.org/10.1080/09243046.2013.847780.
[35] Shi L. Heat transfer in the thick thermoset composites. Technische Univeristeit Delft; 2016. PhD Thesis.
[36] Saffar F, Sonnenfeld C, Beauchêne P, Park CH. In-situ monitoring of the out-of-autoclave consolidation of carbon / poly-ether-ketone-ketone prepreg laminate. Front Mater 2020;7:1–12. https://doi.org/10.3389/fmats.2020.00195.
[37] Han N, Baran I, Zanjani JSM, Yuksel O, An LuLing, Akkerman R. Experimental and computational analysis of the polymerization overheating in thick glass/Elium® acrylic thermoplastic resin composites. Compos Part B Eng 2020;202:108430.
[38] Clayton WA. Constituent and composite thermal conductivities of phenolic-carbon and phenolic-graphite ablators. In: Proc 12th struct struct dyn mater conf, Anaheim, CA, USA; 1971. p. 19–21.
[39] Springer GS, Tsai SW. Thermal conductivities of unidirectional materials. J Compos Mater 1967;1:166–73. https://doi.org/10.1177/002199836700100206.
[40] Shin DD, Hahn HT. Compaction of thick composites: simulation and experiment. Polym Compos 2004;25(1):49–59.
[41] Xue S, Barlow JW. Thermal properties of powders. In: Proc 1990 int solid free fabr symp; 1990. p. 179–85.
[42] Tian X, Peng G, Yan M, He S, Yao R. Process prediction of selective laser sintering based on heat transfer analysis for polyamide composite powders. Int J Heat Mass Transf 2018;120:379–86. https://doi.org/10.1016/J.IJHEATMASSTRANSFER.2017.12.045.
[43] ÉireComposites Teo. GRN 918 Datasheet; 2013.
[44] Hsiao K-T, Laudorn H, Advani SG. Experimental investigation of heat dispersion due to impregnation of viscous fluids in heated fibrous porous during composites processing. J Heat Transfer 2001;123:178–87. https://doi.org/10.1115/1.1338131.
[45] Lee C. An investigation into the transverse thermal conductivity of fibre beds. University of Limerick; 2004. MEng Thesis.
[46] Tan H, Pillai KM. Multiscale modeling of unsaturated flow of dual-scale fiber preform in liquid composite molding II: Non-isothermal flows. Compos Part A Appl Sci Manuf 2012;43:14–28. https://doi.org/10.1016/j.compositesa.2011.06.012.
[47] Toray Carbon Fibers America. T700S Data Sheet; 2019.
[48] Amico S, Lekakou C. Flow through a two-scale porosity, oriented fibre porous medium. Transp Porous Media 2004;54:35–53. https://doi.org/10.1023/A:1025799404038.
[49] Tahir MW, Hallström S, Åkermo M. Effect of dual scale porosity on the overall permeability of fibrous structures. Compos Sci Technol 2014;103:56–62. https://doi.org/10.1016/J.COMPSCITECH.2014.08.008.
[50] Gebart BR. Permeability of Unidirectional Reinforcements for RTM. J Compos Mater 1992;26:1100–33. https://doi.org/10.1177/002199839202600802.
[51] Kuentzer N, Simacek P, Advani SG, Walsh S. Permeability characterization of dual scale fibrous porous media. Compos Part A Appl Sci Manuf 2006;37:2057–68. https://doi.org/10.1016/j.compositesa.2005.12.005.
[52] Manville Johns. Single-end roving selector guide; 2018.
[53] DiBenedetto AT. Prediction of the glass transition temperature of polymers: a model based on the principle of corresponding states. J Polym Sci Part B Polym Phys 1987;25:1949–69. https://doi.org/10.1002/polb.1987.090250914.
[54] Kreyszig E, Kreyszig H, Norminton EJ. Advanced engineering mathematics. 10th ed. Ltd: John Wiley & Sons; 2011.
[55] Kluge NEJ, Lundström TS, Ljung A-L, Westerberg LG, Nyman T. An experimental study of temperature distribution in an autoclave. J Reinf Plast Compos 2016;35:566–78. https://doi.org/10.1177/0731684415624768.
[56] Centea T, Peters G, Hendrie K, Nutt S. Effects of thermal gradients on defect formation during the consolidation of partially impregnated prepregs. J Compos Mater 2017;51:3987–4003. https://doi.org/10.1177/0021998317733317.
[57] Kravchenko OG, Kravchenko SG, Pipes RB. Chemical and thermal shrinkage in thermosetting prepreg. Compos A Appl Sci Manuf 2016;80:72–81.
[58] Oh JH. Prediction of temperature distribution during curing thick thermoset composite laminates. Mater Sci Forum 2007;545:427–30. https://doi.org/10.4028/www.scientific.net/MSF.544-545.427.
[59] Hollaway LC. 20 – Advanced fibre-reinforced polymer (FRP) composite materials for sustainable energy technologies. Adv Fibre-Reinforced Polym Compos Struct Appl, Woodhead Publishing Limited 2013;20:737–79. https://doi.org/10.1533/9780857098641.4.737.